J. Electrochem. Sci. Eng. **16** (2026) 3318; https://doi.org/10.5599/jese.3318

Open Access : : ISSN 1847-9286
https://pub.iapchem.org/ojs/index.php/JESE

Original scientific paper

$NiFe_2O_4$/(S,N)-doped graphene oxide composite as efficient electrochemical sensor for determination of sibutramine in dietary supplements

Ngo Thi Thanh Xuan[1,2], Le Thi Thanh Nhi[3,4] Nguyen Quang Man[5], Vo Thi Khanh Ly[5], Le Thi Hong Phong[6], Nguyen Hai Phong[1], Pham Khac Lieu[1], Le Lam Son[1,✉] and Dinh Quang Khieu[1,✉]

[1]*University of Sciences, Hue University, 530000, Vietnam*
[2]*Drug, Cosmetic and Food Quality Control Center of Hue City, 530000, Vietnam*
[3]*Center for Advanced Chemistry, Institute of Research and Development, Duy Tan University, 03 Quang Trung, Da Nang 550000, Vietnam*
[4]*Faculty of Natural Sciences, Duy Tan University, 03 Quang Trung, Da Nang 550000, Vietnam*
[5]*University of Medicine and Pharmacy, Hue University,530000, Vietnam*
[6]*Institute of Materials Sciences, Vietnam Academy of Science and Technology, 18 Hoang Quoc Viet, Cau Giay, Hanoi City 100000, Vietnam*

Corresponding Authors: ✉ lelamson@hueuni.edu.vn; ✉ dqkhieu@hueuni.edu.vn

Received: March 31, 2026; Accepted: June 22, 2026; Published: June 27, 2026

Abstract

A novel electrochemical sensor based on a $NiFe_2O_4$/(S,N)-doped graphene oxide composite (NiF/GrO(S,N)) was developed to detect sibutramine (SBT). The composite material was successfully synthesized and characterized using X-ray diffraction, Raman spectroscopy, scanning electron microscopy, energy-dispersive X-ray spectroscopy, nitrogen adsorption/ /desorption isotherms, and vibrating sample magnetometry. Results confirmed the formation of a nanocrystalline $NiFe_2O_4$ structure uniformly dispersed on S,N-doped graphene sheets, providing a high surface area and numerous active sites. The NiF/GrO(S,N)-modified glassy carbon electrode (GCE) showed improved electrocatalytic activity toward SBT oxidation. Under optimized conditions, differential pulse voltammetry revealed two linear ranges from 0.5 to 8.9 µM and 8.9 to 19.6 µM, with a detection limit of 0.37 µM. The sensor also demonstrated good repeatability, reproducibility, and stability, along with effective anti-interference capabilities against common inorganic and organic substances. The practical applicability of the proposed sensor was successfully demonstrated by determining SBT in seven commercial dietary supplement samples. The obtained recoveries ranged from 96.38 to 104.83 %, and the results showed no statistically significant difference compared with those obtained using the standard HPLC method. These results suggest that the NiF/GrO(S,N)/GCE sensor is a promising platform for the rapid and reliable detection of SBT in real samples.

Keywords
Anti-obesity drug sensing; nickel ferrite; graphene oxide; heteroatoms doping; differential pulse voltammetry; food supplements

Introduction

Sibutramine ($C_{17}H_{26}ClN$, SBT) is a synthetic anorectic drug that was previously used as an anti-obesity agent due to its appetite-suppressing effect, which acts through the inhibition of neurotransmitter reuptake in the central nervous system [1]. However, numerous studies have reported that SBT may cause serious cardiovascular side effects, including hypertension, tachycardia, and increased risk of heart attack and stroke [2]. As a result, SBT has been banned or strictly regulated in many countries [3]. Despite these regulations, SBT is still frequently detected as an illegal adulterant in dietary supplements and weight-loss products, posing significant health risks to consumers [4,5]. Therefore, the development of reliable and sensitive analytical methods for determining SBT in food and dietary supplement products is of great importance. Several analytical approaches have been reported for SBT determination, including magnetic solid phase extraction combined with HPLC-DAD (high-performance liquid chromatography with diode array detection) [6], green HPLC-PDA method [7] and liquid chromatography-mass spectrometry (LC-MS/MS) [8,9]. Although these techniques provide high accuracy and selectivity, they generally require sophisticated instrumentation, complex sample preparation procedures, and relatively long analysis times. In contrast, electrochemical sensing methods have attracted considerable attention due to their high sensitivity [10], rapid response, simple operation, and low cost [11], making them promising alternatives for routine analysis [12-14].

The performance of electrochemical sensors largely depends on the properties of the electrode modification materials. In recent years, graphene-based materials have been extensively studied because of their excellent electrical conductivity, large specific surface area, and chemical stability [15,16]. Additionally, heteroatom-doped graphene, such as nitrogen- and sulphur-doped graphene, can introduce additional defects and active sites, significantly enhancing the electrocatalytic activity of the electrode surface [17].

Conversely, spinel ferrite nanomaterials such as $NiFe_2O_4$ have gained increasing interest due to their unique physicochemical properties, including high catalytic activity, chemical stability, and magnetic properties [18,19]. Combining ferrite nanoparticles with graphene-based materials can create hybrid nanostructures that leverage the benefits of both components. In these systems, graphene offers a conductive network that enhances electron transfer, while ferrite nanoparticles provide numerous catalytically active sites, leading to improved electrochemical performance [20,21]. Although many graphene-based electrochemical sensors have been developed, the use of $NiFe_2O_4$/ /S,N-doped graphene composites for detecting sibutramine is rarely reported. Developing such hybrid materials could generate a synergistic effect, greatly boosting the sensitivity and electrocatalytic activity of the sensing platform.

In this study, a $NiFe_2O_4$/S,N-doped graphene oxide composite (NiF/GrO(S,N)) was synthesized and employed as a novel electrode-modification material for the electrochemical detection of sibutramine. The electrochemical behaviour of sibutramine at the modified electrode was examined using cyclic voltammetry (CV) and differential pulse voltammetry (DPV). The analytical performance of the proposed sensor was assessed in terms of sensitivity, selectivity, repeatability, and stability. Moreover, the method was successfully applied to detect SBT in commercial dietary supplement samples, demonstrating its potential for practical use in food and pharmaceutical analysis.

(cc) BY

Experimental

Chemicals

Graphite (C, Merck), nickel chloride hexahydrate ($NiCl_2·6H_2O$, 99 %, Merck), and iron(III) chloride hexahydrate ($FeCl_3·6H_2O$, 98 %, Merck) were used as precursors for nickel ferrite synthesis. Sibutramine (SBT) standard solutions were prepared using distilled water. Britton-Robinson buffer solution (BRS, 0.1 M), with varying pH levels, was used as the supporting electrolyte. All solutions were prepared with distilled water.

Synthesis of NiF/GrO (N,S) composite

GrO(S,N) was prepared based on the method reported by Marcano *et al.* [22] with slight modifications. Briefly, 3 g of graphite powder was slowly added to a pre-mixed solution containing concentrated H_2SO_4 (360 mL) and H_3PO_4 (40 mL) while stirring continuously. Subsequently, 18 g of $KMnO_4$ was gradually introduced into the mixture, resulting in a mildly exothermic reaction. Then, 1.5 g of thiourea (as a nitrogen and sulphur precursor) was added, and the mixture was continuously stirred for 72 h. After that, 17 mL of H_2O_2 was slowly added dropwise, and the reaction mixture was allowed to cool to room temperature. The resulting suspension was centrifuged at 4000 rpm for 10 min, and the supernatant was discarded to obtain a brownish-yellow solid. The solid was washed several times with 0.1 M HCl solution and deionized water, followed by centrifugation. Finally, the product was dried at 60 °C for 48 h to obtain a black solid, namely nitrogen and sulphur co-doped graphite oxide (GrO(S,N)).

NiF was synthesized according to the method reported by Askari and Salarizadeh [23]. $FeCl_3·6H_2O$ (2.16 g) and $NiCl_2·6H_2O$ (0.95 g) were dissolved in a mixed solvent of 50 mL deionized water and 30 mL ethanol under magnetic stirring until completely dissolved. Then, 15 mL of 25 % NH_3 solution was added to the mixture, and the mixture was stirred for an additional 60 min. The obtained mixture was subsequently transferred into a Teflon-lined stainless-steel autoclave and subjected to hydrothermal treatment at 180 °C for 12 h. After cooling to room temperature, the precipitate was collected by filtration, washed three times with deionized water and ethanol, and dried at 60 °C for 24 h. The dried product was ground into a fine powder to obtain NiF.

A mixture containing 50 mL of deionized water, 30 mL of ethanol, and 0.3 g of GrO(S,N) was ultrasonically dispersed for 120 min. The suspension was then stirred magnetically for 15 min before adding *m* grams of NiF. The mixture was stirred for an additional 60 min. Afterward, the product was collected by centrifugation at 4000 rpm, washed three times with deionized water and ethanol, and dried at 60 °C for 48 h. The obtained solid was ground into fine powder to yield the composites denoted as (0.5/1)NiF/GrO(S,N), (1.0/1)NiF/GrO(S,N) and (1.5/1)NiF/GrO(S,N), corresponding to NiF amounts (*m*) of 0.15, 0.30 and 0.45 g, respectively.

Apparatus

The crystal structures of the prepared materials were analysed using X-ray diffraction (XRD). Raman spectroscopy was used to investigate the structural characteristics of graphene-based materials. The morphology and elemental composition were examined using a Nova NanoSEM 450 scanning electron microscope (USA) coupled with energy-dispersive X-ray spectroscopy (EDX). The specific surface area and pore structure were evaluated using a Micromeritics Tristar 3000. The magnetic properties of the materials were investigated using a Micro Sense Easy VSM 20130321-02 vibrating sample magnetometer (VSM). Raman spectra were obtained using a Senterra dispersive Raman spectrometer (Bruker) with a 532 nm excitation wavelength. Fourier transform infrared spectroscopy (FT-IR) was used to identify the functional groups present, utilizing an IR Affinity-1S

spectrophotometer (Shimadzu). Electrochemical experiments were performed using a CPA-HH5 workstation (Vietnam), in which a platinum wire, a glassy carbon electrode, and an Ag/AgCl/KCl 3 M electrode were employed as the counter, working, and reference electrode, respectively.

HPLC was additionally employed to analyse sibutramine in real samples for comparison with the electrochemical method (DPV). Sibutramine present in the samples (if any) was extracted using a mixture of acetonitrile and 50 mM ammonium dihydrogen phosphate buffer (pH 6.0) in a ratio of 70:30 (v/v), and the resulting extract was injected into the HPLC system. The HPLC conditions were as follows: detection was performed using a photodiode array (PDA) detector set at the maximum absorption wavelength of 223 nm; the mobile phase consisted of acetonitrile and 50 mM ammonium dihydrogen phosphate buffer (pH 6.0) (70:30, v/v); chromatographic separation was carried out on a reversed-phase C18 column (250×4.6 mm, 5 µm particle size); the flow rate was maintained at 1.5 mL min^{-1}; and the injection volume was 20 µL.

Preparation of modified GC electrode and electrochemical measurements

Prior to modification, the glassy carbon electrode (GCE) was polished with alumina slurry and thoroughly rinsed with distilled water. A suspension of the NiF/GrO(S,N) composite was prepared by dispersing the material in distilled water under ultrasonic treatment. A volume of the suspension (1 to 10 µL) was dropped onto the cleaned GCE surface and allowed to dry at room temperature, forming the NiF/GrO(S,N) modified electrode. Electrochemical experiments were performed using cyclic voltammetry (CV) and differential pulse voltammetry (DPV). The measurements were carried out in 0.1 M BRS buffer solution (pH 3) under optimized conditions.

To determine SBT, the modified electrode was immersed in a supporting electrolyte containing different concentrations of SBT, and the oxidation peak currents were recorded. The calibration curve was obtained by plotting the peak current against SBT concentration.

Real sample preparation and analysis

Five units of each dietary supplement sample were accurately weighed to determine the average mass per unit, and then finely ground into powder. An appropriate amount of the powdered sample was transferred into a 100 mL volumetric flask, dissolved in distilled water, and sonicated for 15 min to ensure complete extraction. The resulting suspension was filtered, and the filtrate was further diluted 10-fold with distilled water to obtain the stock test solution for electrochemical analysis.

An aliquot of 3 mL of the stock test solution was accurately transferred into the electrochemical cell, followed by the addition of 0.1 M buffer solution (pH 3) to a final volume of 20 mL. The measurement was then carried out under the optimized conditions described above to determine the SBT content of the samples.

Standard addition method (recovery test): An aliquot of 3 mL of the stock test solution was transferred into the electrochemical cell, followed by the addition of 5 µL of SBT standard solution (10^{-3} M). The solution was then diluted to 20 mL with 0.1 M buffer (pH 3) and analysed under the same optimized conditions. The recovery was calculated by comparing the added and measured amounts of SBT.

Results and discussion

Material characterization

The XRD pattern of $NiFe_2O_4$ shows characteristic diffraction peaks at about 30.2, 35.5, 43.2, 53.5, 57.1 and 62.7°, corresponding to the (220), (311), (400), (422), (511) and (440) crystal planes of cubic spinel $NiFe_2O_4$ (JCPDS No. 10-0325) (Figure 1A). These clear diffraction peaks confirm the successful

(cc) BY

formation of crystalline $NiFe_2O_4$ with a typical spinel structure. The GrO sample displays a diffraction peak cantered at 10.5° and a broad peak cantered at 26° , respectively, which are assigned to the (001) and (002) planes of graphene oxide [24]. After S,N doping, the diffraction peaks become broader and weaker, and shift to higher diffraction angles, suggesting an increase in structural defects and disorder in the graphene framework due to the incorporation of heteroatoms.

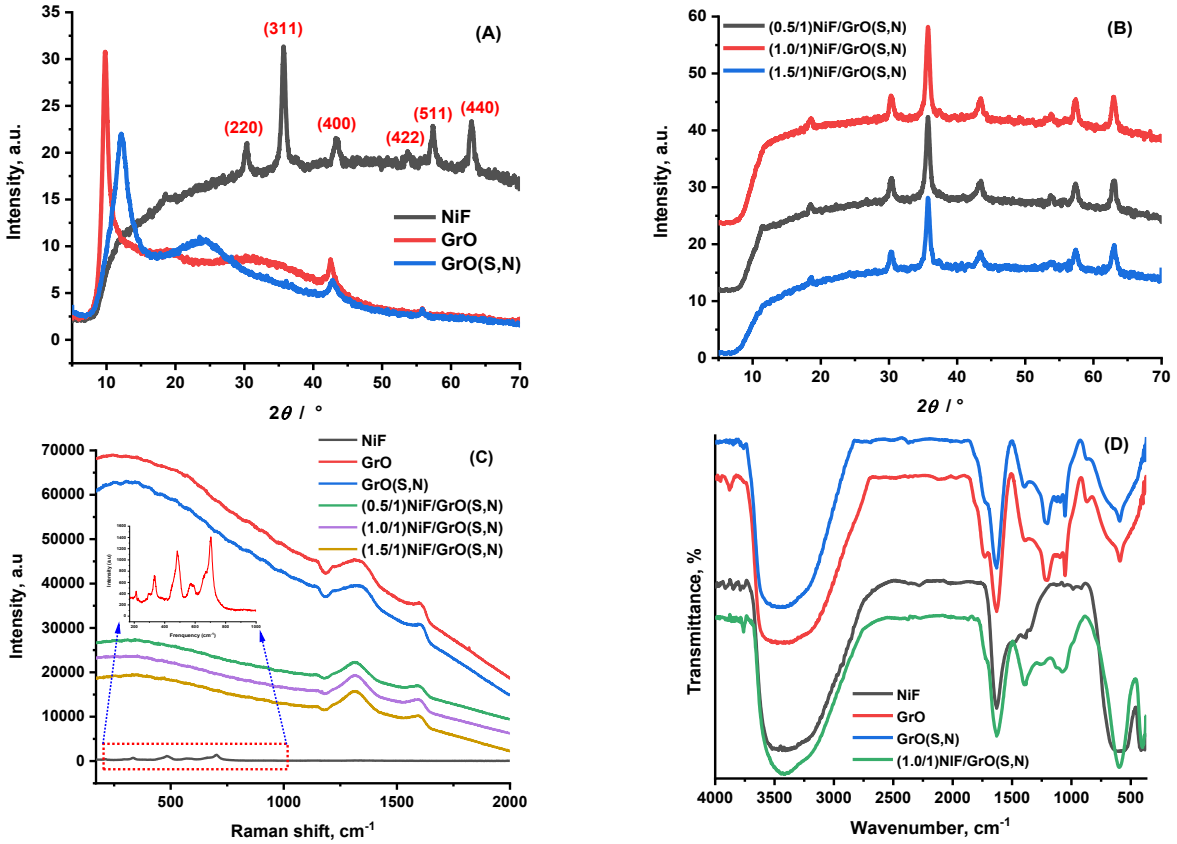

Figure 1. *XRD patterns of A - NiF, GrO, and GrO(S,N) and B - NiF/rGO(S,N) composites with different mass ratios; C - Raman spectra of NiF, GrO, GrO(S,N), and NiF/GrO(S,N) composites (the inset shows the characteristic Raman modes of NiF); D - FTIR spectra of NiF, GrO, GrO(S,N), and (1.0/1) NiF/GrO(S,N) composites*

For the $NiFe_2O_4$/GrO(S,N) composites with different ratios (0.5:1, 1:1 and 1.5:1), the characteristic diffraction peaks of $NiFe_2O_4$ remain clearly visible without the appearance of additional impurity peaks, indicating that the crystal structure of $NiFe_2O_4$ is preserved after composite formation (Figure 1B). The characteristic peak of GrO is not clearly observed in the composite due to its relatively low content and the strong diffraction intensity of $NiFe_2O_4$ or is partially converted to reduced graphene oxide.

The average crystallite size of $NiFe_2O_4$ was further estimated using the Scherrer equation $D = K\lambda/\beta\cos\theta$ based on the most intense (311) diffraction peak at approximately 35.5°, where $K = 0.9$, $\lambda = 0.15406$ nm (Cu Kα radiation), β is the full width at half maximum (FWHM) of the diffraction peak in radians, and θ is the Bragg angle. The calculated crystallite size is 11-12 nm, which is in the nanometre range, confirming the nanocrystalline nature of the synthesized $NiFe_2O_4$. Such nanoscale crystallites are beneficial for improving the interfacial contact and charge transfer in the composite material.

Raman spectroscopy was used to investigate the structural features of NF and its composites. As shown in Figure 1C, the Raman spectrum of NiF exhibits several characteristic vibrational modes at approximately 213, 332, 483, 569, 703 cm^{-1}, which can be assigned to the F_{2g}, E_g, F_{2g}, F_2 and A_{1g} modes of

the spinel ferrite structure [25]. These peaks are typical Raman-active modes of NiF and confirm the formation of the spinel phase. For GrO and GrO(S,N), two prominent bands are observed at approximately 1350 cm^{-1} (D band) and 1580 cm^{-1} (G band), corresponding to the breathing mode of sp^2 carbon rings and the in-plane vibration of sp^2 carbon atoms, respectively [26]. The intensity ratio I_D/I_G is commonly used to evaluate the degree of structural disorder in graphene-based materials. The I_D/I_G ratio increases from 1.86 for GrO to 1.95 for GrO-N,S, indicating that the incorporation of S and N heteroatoms introduces additional defects and distortion in the graphene lattice. After the introducetion of $NiFe_2O_4$ nanoparticles, the I_D/I_G values further increase to 2.39, 2.46 and 2.53 for the composites with different $NiFe_2O_4$ loadings. This result suggests that the interaction between $NiFe_2O_4$ and the graphene framework generates more defect sites and structural disorder. Such defect-rich structures are beneficial for enhancing surface activity and facilitating charge transfer within the composite material.

The FTIR spectra of GrO, GrO(S,N), NiF and the NiF/GrO(S,N) composites are shown in Figure 1D. For GrO, the broad band at ~3416 cm^{-1} is attributed to O-H stretching vibrations, indicating the presence of hydroxyl groups and adsorbed water. The peak at ~1782 cm^{-1} corresponds to C=O stretching of carboxyl groups, while the bands at ~1215 and ~1048 cm^{-1} are assigned to C-O-C (epoxy) and C-OH (hydroxyl) vibrations, respectively, confirming the successful oxidation of graphite [27]. After doping, the FTIR spectrum of GrO(S,N) exhibits noticeable changes. The band in the region of ~1200 to 1300 cm^{-1} may arise from overlapping contributions of C-N and C-O vibrations, suggesting possible incorporation of nitrogen-containing functional groups into the graphene oxide framework [28]. Additionally, a band observed around ~600 to 700 cm^{-1} can be tentatively associated with C-S vibrations; however, overlap with metal-oxygen vibrations cannot be excluded [29]. For NiF, characteristic absorption bands at ~596 and ~396 cm^{-1} are observed, corresponding to Fe-O and Ni-O vibrations at tetrahedral and octahedral sites, respectively, confirming the formation of the spinel $NiFe_2O_4$ structure. In the NiF/GrO(S,N) composites, the coexistence of characteristic bands from both GrO(S,N) and NiF is clearly observed. Slight shifts and changes in the intensity of several bands, particularly in the regions associated with oxygen-containing groups and metal-oxygen vibrations, indicate possible interfacial interactions between $NiFe_2O_4$ and the doped graphene oxide matrix.

The textural properties of the materials were evaluated using N_2 adsorption-desorption measurements. As shown in Figure 2A, the adsorption-desorption isotherms display typical type IV behaviour with a sharp increase at high relative pressure ($P/P_0 > 0.8$), indicating the presence of mesoporous structures. The specific surface area of GrO is 78.0 $m^2\ g^{-1}$, while that of GrO(S,N) decreases to 13.7 $m^2\ g^{-1}$, likely due to partial restacking of graphene sheets during the doping process (Table 1). Pure $NiFe_2O_4$ exhibits a moderate surface area of 29.2 $m^2\ g^{-1}$. After forming composites with GrO(N,S) the surface areas increase significantly to 77 to 82 $m^2\ g^{-1}$, indicating that the dispersion of ferrite nanoparticles effectively prevents graphene restacking and generates additional porous structures. The coexistence of micro- and mesopores facilitates mass transport and provides abundant active sites. The magnetic properties of the materials were investigated using vibrating sample magnetometry (VSM) at room temperature (Figure 2B). The magnetization curves exhibit typical S-shaped hysteresis loops, confirming the ferrimagnetic nature of the materials. Pure NiF shows a saturation magnetization (M_s) of 48.8 A $m^2\ kg^{-1}$, with a remanent magnetization (M_r) of 2.1 A $m^2\ kg^{-1}$ and coercivity (Hc) of 1878.6 A m^{-1}. After hybridization with graphene-based materials, the M_s values decrease to 16.4 to 29.7 A $m^2\ kg^{-1}$, a decrease attributable to the presence of non-magnetic graphene components (Table 1). Nevertheless, the composites exhibit clear magnetic responses and relatively low coercivity (~1711.4 to 1854.7 A m^{-1}), indicating typical soft magnetic behaviour characteristic of nanoscale materials.

(cc) BY

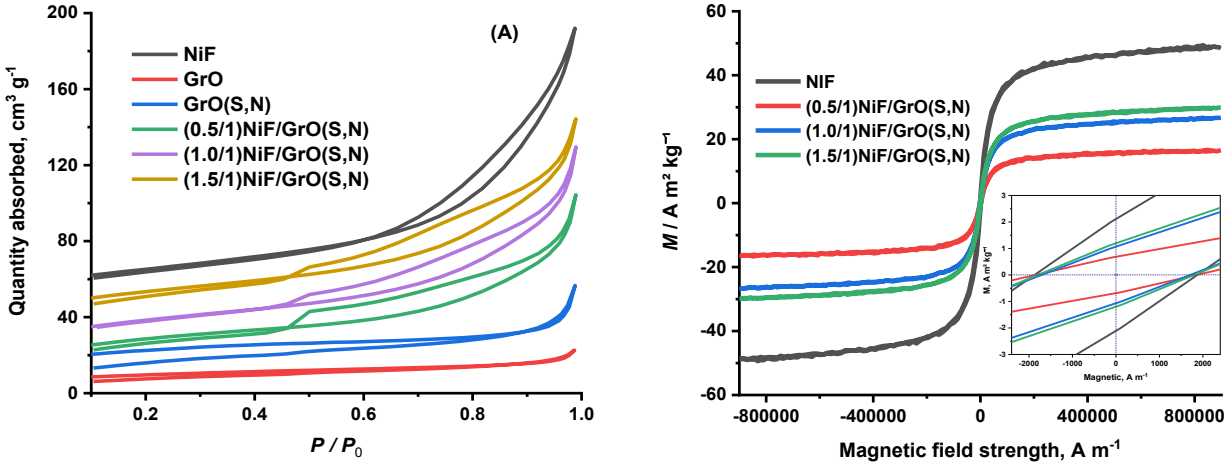

***Figure 2**. A - N_2 adsorption-desorption isotherms of NiF, GrO, GrO(S,N) and NiF/GrO(S,N) composites with different mass ratios and B - magnetic hysteresis loops of NiF and NiF/GrO(S,N) composites measured at room temperature (the inset shows the enlarged view of the low-field region)*

***Table 1**. Structural, textural and magnetic properties of GrO, GrO(S,N), NiF and NiF/GrO(S,N) composites*

Materials	Crystallite size, nm*	S_{BET} / m² g⁻¹	$S_{micropore}$ / m² g⁻¹	$S_{mesopore}$ / m² g⁻¹	SM		
					M_s / A m² kg⁻¹	M_r / A m² kg⁻¹	H_c / A m⁻¹
GrO	-	78.0053	2.5163	75.489	-	-	-
GrO(S,N)	-	13.7121	-	13.7121	-	-	-
NiF	11.64	29.1629	5.7251	23.4378	48.8	2.1	1878.6
(0.5/1)NiF/GrO(S,N)	11.10	79.0962	31.1862	47.91	16.4	0.7	1854.7
(1.0/1) NiF/GrO(S,N)	11.57	77.426	13.4746	63.9514	26.5	1.1	1711.4
(1.5/5) NiF/GrO(S,N)	11.56	81.9682	15.7761	66.1921	29.7	1.2	1799.0

*Crystallite size from Scherrer equation (311 peak)

The elemental distribution of the NiF/GrO(S,N) composite was further analysed using EDX (Figure 3) and EDX elemental mapping (Figure 4). As shown in Figure 4, the mapping images display the presence and spatial distribution of Ni, Fe, O, C, N, and S across the examined area. The homogeneous distribution of Fe and Ni suggests a uniform dispersion of NIF nanoparticles within the composite. The C signal (14.44 wt.%) stems from the graphene framework, while the O (22.65 wt.%), Fe (44.4 wt.%) and Ni (17.96 wt.%) signals mainly relate to the metal-oxygen bonds in the ferrite structure and residual oxygen-containing groups in graphene. Additionally, the S (0.40 wt.%) and N (0.15 wt.%) signals, although present at low levels, are clearly detected and spread over the graphene sheets, indicating successful incorporation of heteroatoms into the graphene structure.

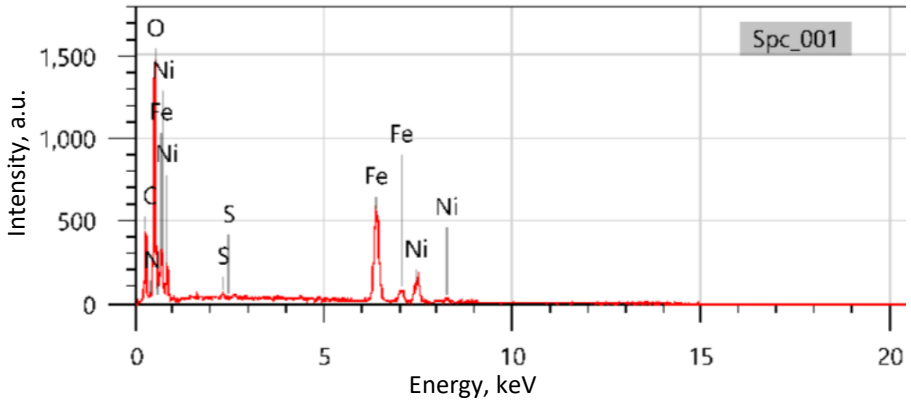

***Figure 3.** EDX spectrum of the NiF/GrO(S,N) composite. Spc_001 denotes the selected analysis area (Spectrum 001) used for EDX measurement*

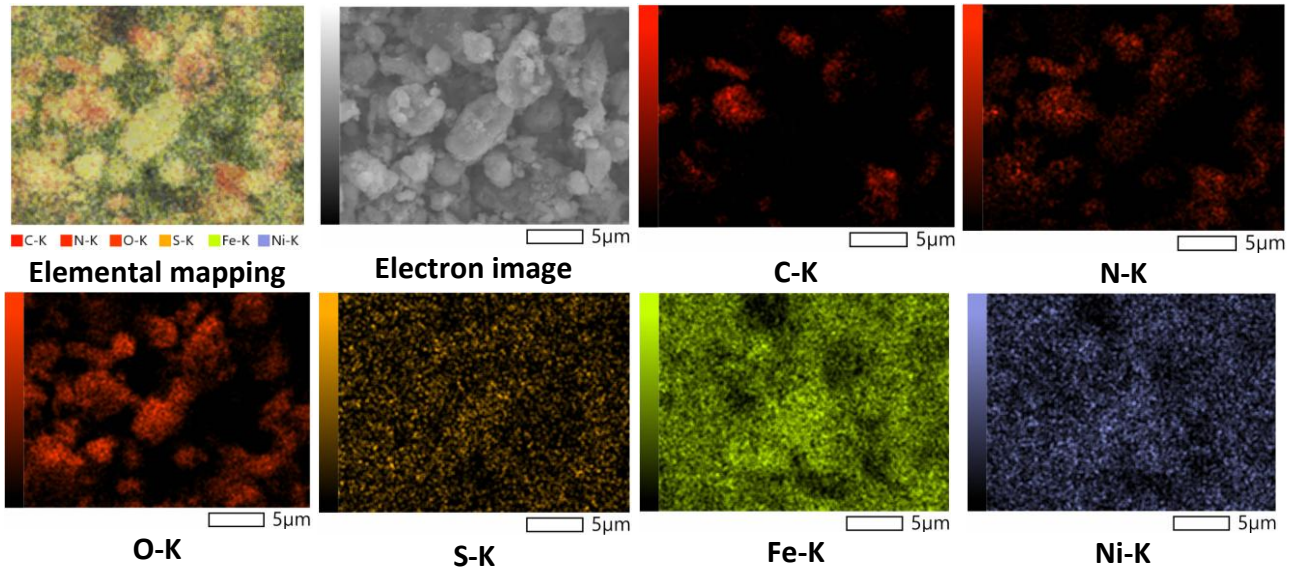

Figure 4. *EDX elemental mapping images of the NiF/GrO(S,N) composite showing the spatial distribution of Ni, Fe, O, C, N and S elements*

The morphologies of the synthesized materials were investigated by SEM and are presented in Figure 5. As seen in the SEM image in Figure 5A, the GrO sample displays typical wrinkled and crumpled sheet-like structures, confirming the successful formation of graphene oxide. After S,N doping, the (GrO) sheets become rougher and more defective, potentially providing more active sites (Figure 5B).

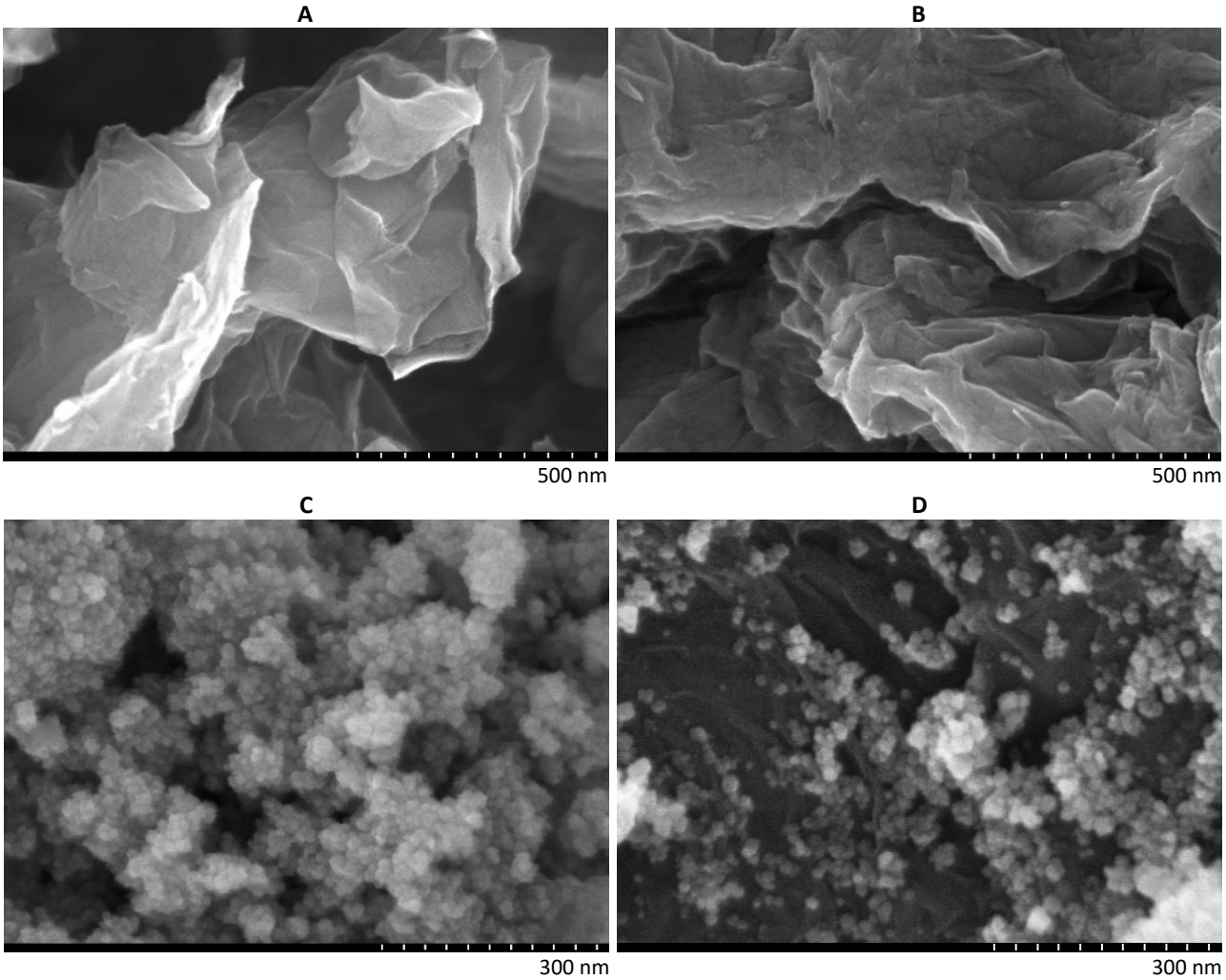

Figure 5*. SEM images of: A - GrO; B - GrO(S,N); C - NiF and D - NiF/GrO(S,N) composite*

(cc) BY

The SEM image in Figure 5C shows that NiF consists of aggregated quasi-spherical nanoparticles measuring tens of nanometers. In the Ni/GrO(S,N) composite, NiF nanoparticles are evenly anchored on the surface of the GrO(S,N) sheets (Figure 5D). The two-dimensional graphene network effectively prevents ferrite nanoparticle aggregation and creates a conductive pathway, which enhances electron transfer and supports electrochemical applications.

Electrochemical determination of SBT using NiF/GrO(S,N)

Electrochemical behaviour of different electrodes

Figure 6A presents the cyclic voltammograms recorded for SBT oxidation at different modified electrodes. Compared with the bare GCE, all modified electrodes exhibited enhanced anodic currents, indicating that the introduction of graphene-based materials and $NiFe_2O_4$ nanoparticles improves the electrocatalytic oxidation of SBT. The oxidation peak current increased from approximately 2.1 μA at GCE to 4.9 μA at GrO and 6.4 μA at GrO(S,N), demonstrating the beneficial effect of N,S co-doping (Figure 6B). Although GrO(S,N) possesses a considerably lower BET surface area (13.71 $m^2 g^{-1}$) than GrO (78.01 $m^2 g^{-1}$), its electrochemical response is significantly higher. This result suggests that electrocatalytic activity is governed not solely by the physical surface area but also by heteroatom-induced defects and active sites, which facilitate electron transfer and analyte adsorption. Upon incorporation of $NiFe_2O_4$, the oxidation current increased substantially owing to the synergistic interaction between the conductive GrO(S,N) matrix and the redox-active $NiFe_2O_4$ nanoparticles. As shown in Figure 6B, the peak current increased from 11.2 μA for (0.5/1)NiF/GrO(S,N) to 15.0 μA for (1.0/1)NiF/GrO(S,N), before decreasing to 13.1 μA for (1.5/1)NiF/GrO(S,N). The enhanced performance of the composite electrodes can be attributed to the combination of efficient charge transport from GrO(S,N) and the abundant catalytic centers provided by $NiFe_2O_4$.

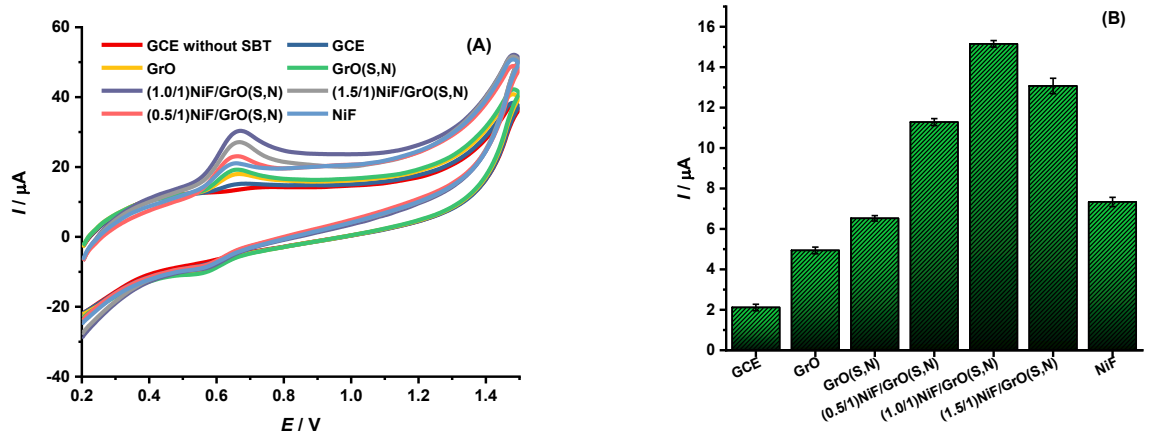

Figure 6. *A - Cyclic voltammograms of GCE and different modified electrodes in 0.1 M BRS buffer solution (pH 3) containing 10 μM SBT at a scan rate of 0.1 V s^{-1}; B - comparison of peak currents obtained at different electrodes (*n *= 3)*

To further elucidate the origin of this behaviour, the electrochemically active surface area (ECSA) was determined using the Randles-Ševčík equation [30] (Figures S1 and S2 of Supplementary material). The ECSA values increased from 0.0348 cm^2 for GCE and 0.0634 cm^2 for GrO(S,N) to 0.0820 cm^2 and 0.0890 cm^2 for (0.5/1)NiF/GrO(S,N) and (1.0/1)NiF/GrO(S,N), respectively, before decreasing to 0.0771 cm^2 for (1.5/1)NiF/GrO(S,N). Notably, the variation in peak current closely follows the ECSA trend, indicating that the electrochemical response is primarily governed by the number of electrochemically accessible active sites rather than by the total physical surface area. A comparison between BET and ECSA data provides additional insight into the structure-performance

relationship. Although (1.5/1)NiF/GrO(S,N) exhibits the highest BET surface area (81.97 $m^2\ g^{-1}$) and mesoporous surface area (66.19 $m^2\ g^{-1}$), its oxidation current and ECSA are lower than those of (1.0/1)NiF/GrO(S,N). This discrepancy indicates that a larger nitrogen adsorption surface area does not necessarily translate into a larger electrochemically active surface. At excessive $NiFe_2O_4$ loading, partial aggregation of nanoparticles and coverage of conductive graphene domains may occur, reducing the fraction of electrochemically accessible sites and hindering charge transfer. Consequently, only a portion of the physical surface area effectively participates in the electrochemical process. Furthermore, the mesoporous structure appears to play a crucial role in facilitating electrolyte penetration and analyte diffusion. The mesoporous surface area increases markedly from 13.71 $m^2\ g^{-1}$ for GrO(S,N) to 47.91 to 66.19 $m^2\ g^{-1}$ for the $NiFe_2O_4$-containing composites, thereby improving mass transport toward the catalytic sites. Among the investigated materials, (1.0/1)NiF/GrO(S,N) provides the most favourable balance between mesoporosity, electrochemically active surface area, and catalytic site density. Therefore, this composite exhibits the highest oxidation current toward SBT and was selected as the optimal electrode material for subsequent electroanalytical investigations.

Effect of the suspension volume

The effect of the suspension volume of (1.0/1)NiF/GrO(S,N) on the electrochemical response toward SBT was investigated by cyclic voltammetry. As shown in Figure 7A, the oxidation peak current gradually increases as the suspension volume increases from 1 to 5 µL, indicating that a larger amount of active material on the electrode surface provides more catalytic sites for the electrochemical reaction. When the suspension volume exceeds 5 µL**,** the peak current slightly decreases. This behaviour can be attributed to the formation of an excessively thick modifier layer on the electrode surface, which may hinder electron transfer and mass transport of the analyte. As summarized in Figure 7B, the maximum peak current is observed at 5 µL, suggesting that this volume provides the optimal balance between the number of active sites and electron-transfer efficiency. Therefore**,** 5 µL was selected as the optimal suspension volume for the preparation of the modified electrode in subsequent experiments.

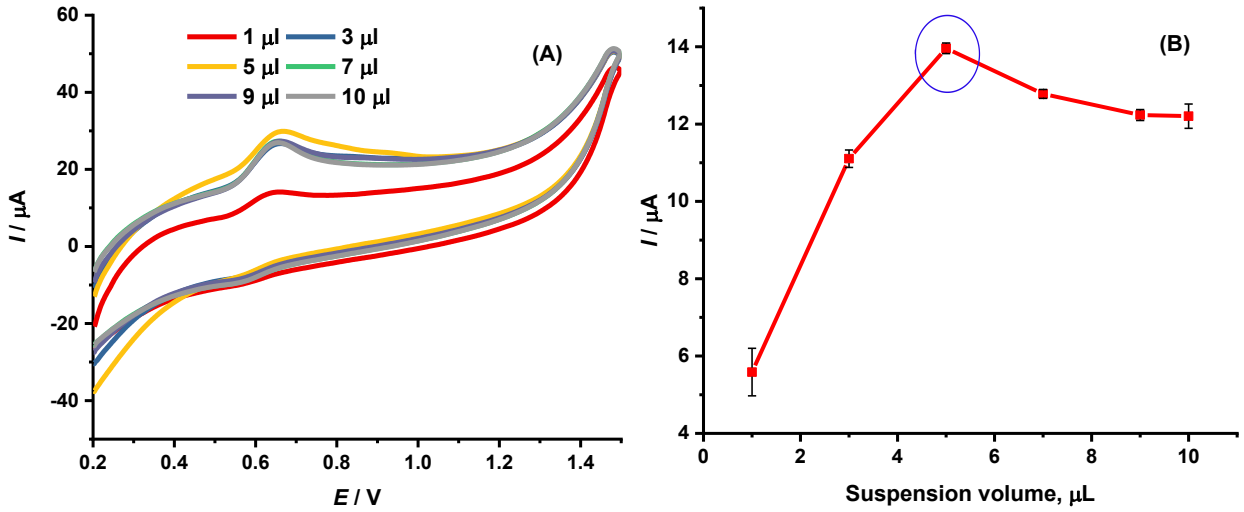

Figure 7. *A - Cyclic voltammograms obtained at the (1.0/1)NiF/GrO(S,N) modified GCE with different suspension volumes (1-10 µL) in 0.1 M BRS buffer solution (pH 3) containing 10 µM SBT at a scan rate of 0.1 V* s^{-1}*; B - dependence of the oxidation peak current on the suspension volume (*n *= 3)*

Effect of pH

The influence of solution pH on the electrochemical oxidation of SBT at the (1.0/1)NiF/GrO(S,N)/ /GCE was investigated in 0.1 M BRS buffer solution over the pH range of 2 to 9, as shown in Figure 8A.

(cc) BY

The oxidation peak current initially increases with pH and reaches a maximum at pH 3, then gradually decreases at higher pH values (Figure 8B). The decrease in peak current at higher pH may be attributed to reduced proton availability and changes in the protonation state of SBT, which can affect electron transfer. Therefore, pH 3 was selected as the optimal pH for subsequent electrochemical measurements.

In addition, the oxidation peak potential shifts negatively with increasing pH, indicating that protons participate in the electrochemical oxidation process. As shown in Figure 8C, a linear relationship between the peak potential (E_p) and pH is obtained using Equation (1):

E_{SBT} = (0.802 ± 0.010) + (-0.050 ± 0.002) pH; R^2 = 0.993 (1)

The slope of approximately 0.050 V pH^{-1} is close to the theoretical Nernst value of 0.059 V pH^{-1}, suggesting that the number of protons involved in the reaction is equal to the number of electrons. Therefore, the electrochemical oxidation of SBT at the (1.0/1)NiF/GrO(S,N)/GCE likely involves one electron and one proton in the rate-determining step.

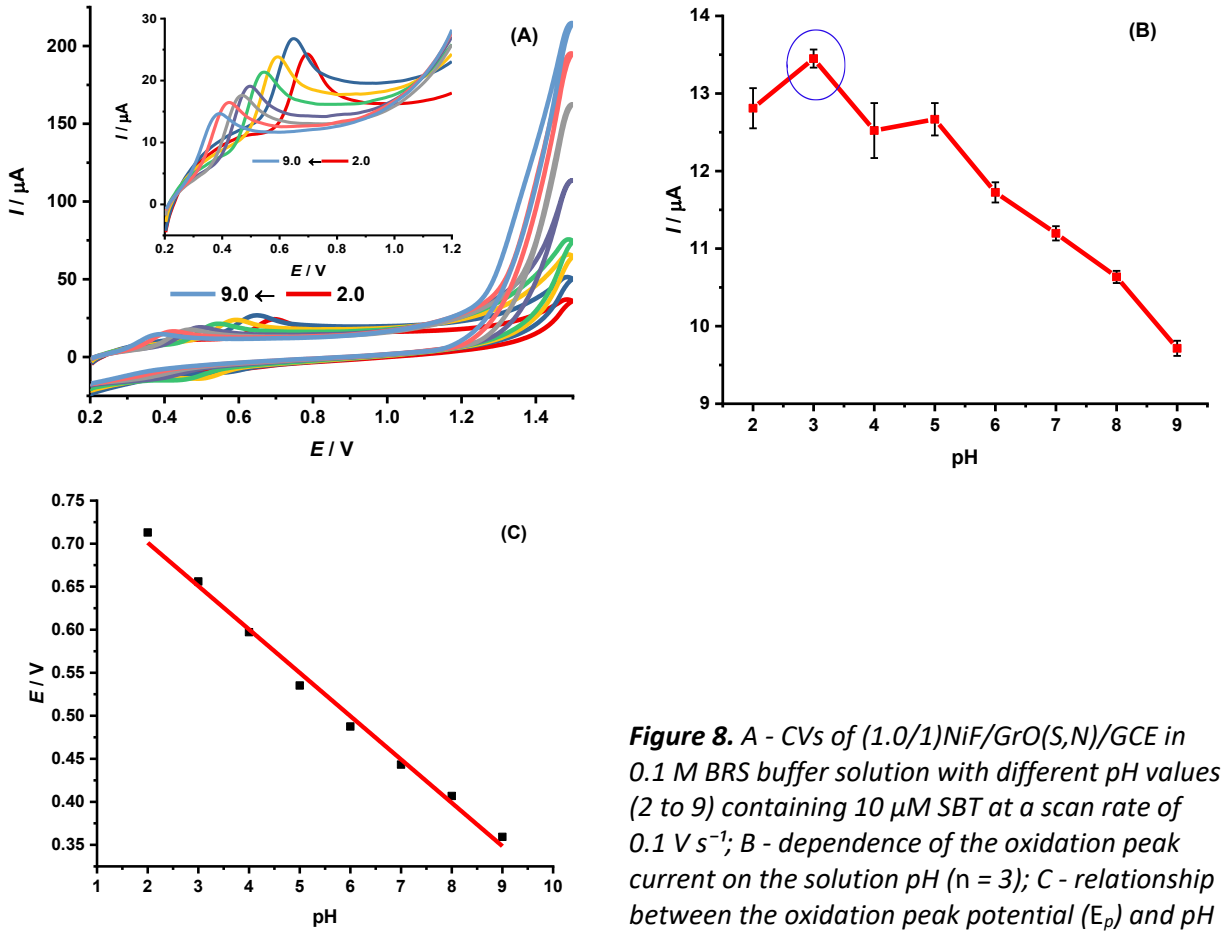

Figure 8. *A - CVs of (1.0/1)NiF/GrO(S,N)/GCE in 0.1 M BRS buffer solution with different pH values (2 to 9) containing 10 µM SBT at a scan rate of 0.1 V s^{-1}; B - dependence of the oxidation peak current on the solution pH (n = 3); C - relationship between the oxidation peak potential (E_p) and pH*

Effect of scan rate

The effect of scan rate on the electrochemical oxidation of SBT at the (1.0/1)NiF/GrO(S,N)/GCE was investigated by cyclic voltammetry in the scan rate range of 0.050 to 0.400 mV s^{-1}, as shown in Figure 9A. As the scan rate increases, the oxidation peak current gradually increases, indicating a faster electrochemical response. As shown in Figure 9B, a good linear relationship is obtained between the oxidation peak current and the square root of the scan rate: I_p = (−2.456 ± 0.363) + + (40.694 ± 0.819)$v^{1/2}$ (R^2 = 0.997), suggesting that the electrochemical process is mainly diffusion-controlled [30,31].

To further clarify the electrochemical mechanism, the relationship between log *I* and log *v* was analysed (Figure 9C), yielding Equation (2):

$$\log I_p = (1.620 \pm 0.014) + (0.611 \pm 0.016) \log v \ (R^2 = 0.994) \quad (2)$$

The slope of 0.611 is close to the theoretical value of 0.5, indicating that the electrochemical oxidation of SBT is predominantly diffusion-controlled, with a partial contribution from adsorption [32].

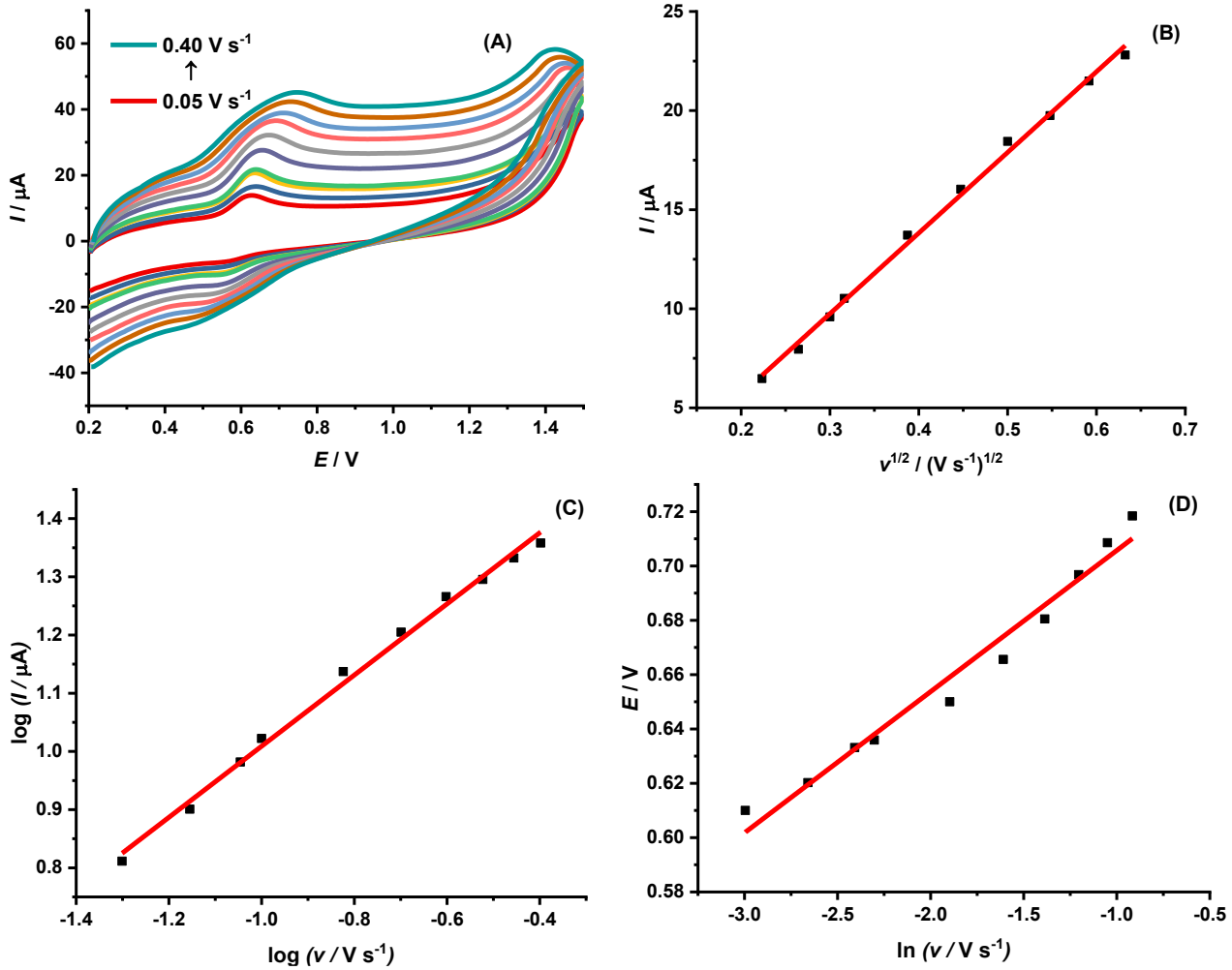

Figure 9. *A - Cyclic voltammograms of (1.0/1)NiF/GrO(S,N)/GCE in 0.1 M BRS buffer solution (pH 3) containing 10 µM SBT at different scan rates (0.05 to 0.40 V* s^{-1}*); B - linear relationship between the oxidation peak current and the square root of the scan rate (*$v^{1/2}$*); C - plot of log* I versus *log* v*; and D - dependence of the oxidation peak potential (*E_p*) on ln* v

Furthermore, the relationship between the oxidation peak potential and the natural logarithm of the scan rate is shown in Figure 9C:

$$E_{SBT} = (0.758 \pm 0.006) + (0.052 \pm 0.003) \ln v; \ R^2 = 0.973 \quad (3)$$

According to Laviron's theory for irreversible electrochemical processes [31], the slope of 0.0512 V obtained from the plot corresponds to an nα value of 0.49. For an irreversible system, the charge transfer coefficient (*α*) is often assumed to be 0.5 [33]; therefore, the number of electrons (*n*) involved in the rate-determining step is estimated to be approximately 0.98 (about 1). This result indicates that one electron participates in the electrochemical oxidation process. Additionally, the pH-dependent study shows that the slope of E_p versus pH is close to the theoretical Nernstian value, suggesting that *n* equals the number of protons (*p*). Consequently, the electrochemical oxidation of SBT is inferred to involve one electron and one proton. Based on these findings, the oxidation mechanism of SBT at the modified GCE can be attributed to protonation of the tertiary amine group, followed by electron

(cc) BY

transfer. In this mechanism, one amine group of the SBT molecule is oxidized, losing one electron and one proton, consistent with previously reported results [34], as shown in Scheme 1.

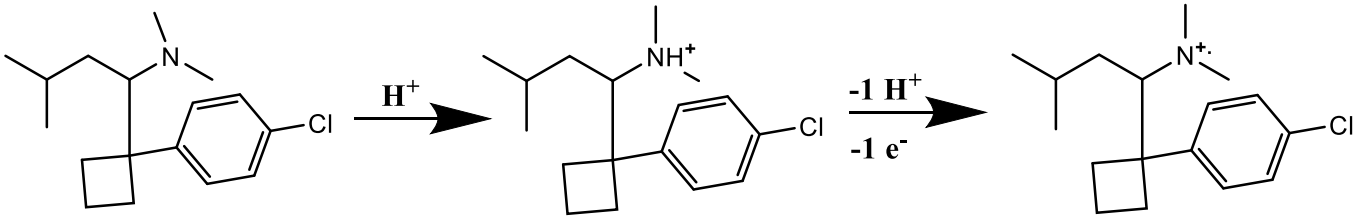

Scheme 1. *The proposed oxidation mechanism of SBT*

Optimized operational parameters

Several important instrumental parameters, including accumulation potential, accumulation time, pulse amplitude, and potential step, were systematically optimized. The results indicate that the optimal conditions are an accumulation potential of 0.4 V, an accumulation time of 5 s, a pulse amplitude of 0.10 V, and a potential step of 0.007 V. Under these conditions, a high and stable peak current was achieved, as illustrated in Figures S3 to S6. These optimized parameters were used for all subsequent experiments.

Linear range and limit of detection

The analytical performance of the (1.0/1)NiF/GrO(S,N)/GCE toward SBT detection was evaluated using differential pulse voltammetry (DPV). As shown in Figure 10A, the oxidation peak current gradually increases with increasing SBT concentration from 0.5 to 19.6 µM, indicating a clear electrochemical response of the modified electrode toward SBT. As presented in Figure 10B, two linear ranges are obtained. In the lower concentration range of 0.5 to 8.9 µM, the peak current exhibits a linear relationship with SBT concentration described by Equation (4):

$$I_p = (2.978 \pm 0.075) + (1.584 \pm 0.014)\, C_{SBT}\ (R^2 = 0.999) \quad (4)$$

In the higher concentration range of 8.9 to 19.6 µM, the calibration Equation (5):

$$I_p = (13.561 \pm 0.048) + (0.377 \pm 0.003)\, C_{SBT}\ (R^2 = 0.999) \quad (5)$$

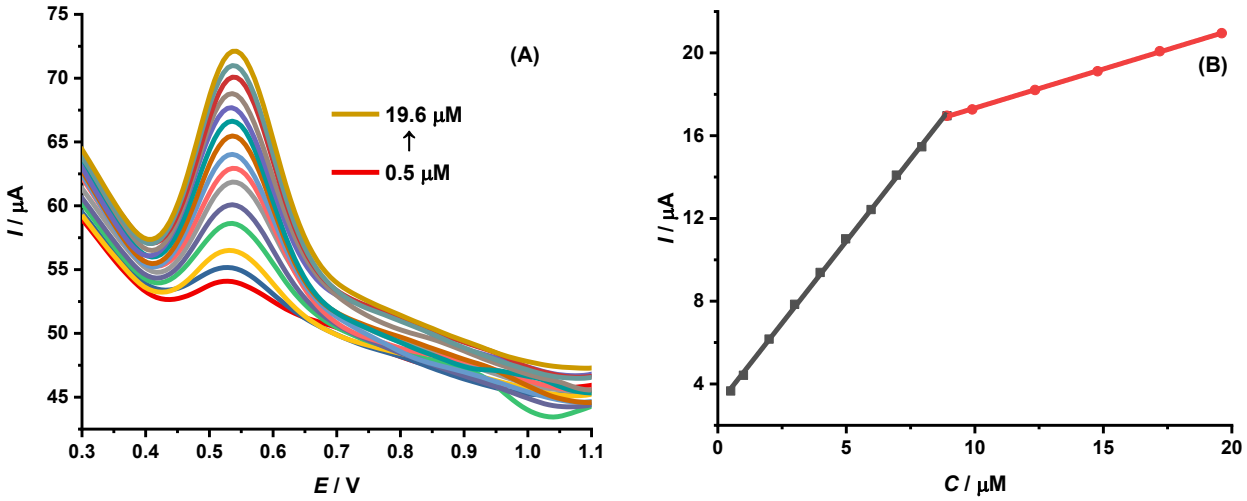

***Figure* 10.** *A - DPVs of (1.0/1)NiF/GrO(S,N)/GCE in 0.1 M BRS buffer solution (pH 3) with different concentrations of SBT (0.5 to 19.6 µM), B - calibration plot of the oxidation peak current versus SBT concentration*

The decrease in slope at higher concentrations can be attributed to partial saturation of active sites on the electrode surface and diffusion limitations. The limit of detection (LOD), estimated according to the 3SD/b criterion (where SD is the standard deviation of the regression and *b* is the

slope of the calibration curve), was found to be 0.37 µM, indicating that the proposed sensor exhibits good sensitivity for SBT detection. The analytical performance of the proposed sensor was compared with that of previously reported electrochemical methods for determining the target analyte. As summarized in Table 2, the detection limit achieved in this work is comparable to or lower than those reported in earlier studies.

***Table 2**. Comparison of analytical performance with previous reports*

Electrode	Method	Linear range, µM	LOD, µM	Samples	Ref.
Carbon graphite screen-printed electrode (SPE-Gr)	AdSDPV	2.0 to 120.0	0.3	Slimming tea beverages	[35]
Mercury working electrode (HMDE)	DPV	5.0 to 117.9	1.4	Beverages and pharmaceutical formulations	[36]
Sibutramine (SBT^+) ion-selective electrode (ISE)	Flow injection analysis	10 to 1000	7.9	Pharmaceutical formulations	[37]
Boron-doped diamond (BDD)	SWV	17.9 to 178.7	0.3 to 6.9	Natural products and multivitamins supplements	[38]
Paper-based electro-chemical device (ePAD)	SWV	9.0 to 299.1	8.8	Capsules, slimming coffee pow-ders and nutraceutical beverages	[39]
NIF/GrO(S,N)/GCE	DPV	0.5 to 8.9; 8.9 to 19.6	0.37	Dietary supplement products	This work

Repeatability, reproducibility and long-term stability

The reliability of the proposed sensor was evaluated with respect to repeatability, reproducibility, and long-term stability (Figure 11).

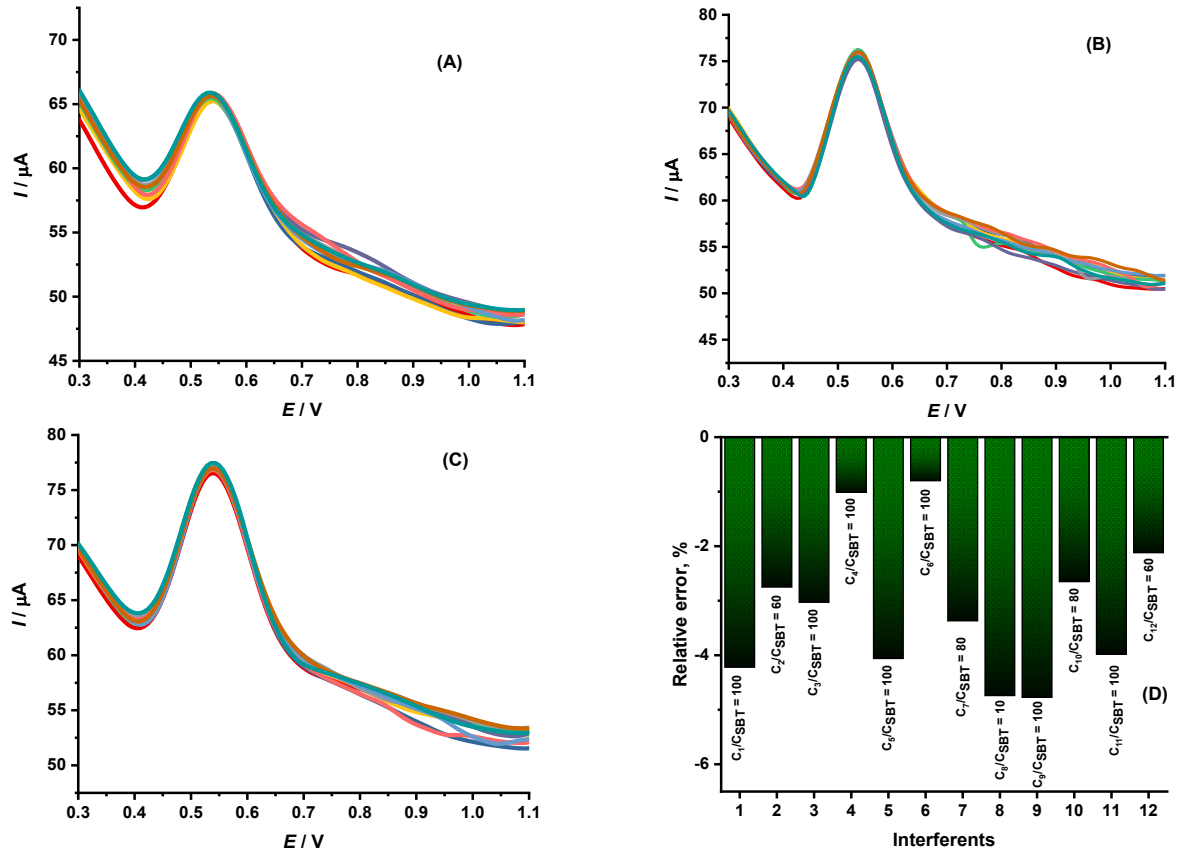

***Figure 11.** DPVs at (1.0/1)NiF/GrO(S,N)/GCE in BRS 0.1 M (pH 3) with C_{SBT}, A - 5.0 , B - 8.9 and C - 19.6 µM (differently coloured curves represent individual replicate scans recorded under identical experimental conditions) and D - interfering study for 12 substances*

The repeatability of the proposed (1.0/1)NiF/GrO(S,N)/GCE sensor was evaluated by performing ten consecutive DPV measurements at three different SBT concentrations (5.0, 8.9, and 19.6 µM).

(cc) BY

The corresponding peak currents were recorded, and the relative standard deviations (RSD) were calculated and compared with the RSD of the Horwitz function (RSDH). At a concentration of 5.0 µM, the average peak current was 11.84±0.57 µA with an RSD of 4.85 %, which is lower than ½RSDH (7.61 %), indicating good repeatability of the measurement. For 8.9 µM SBT, the average peak current was 16.51±0.37 µA, giving an RSD of 2.24 %, which is also smaller than ½RSDH (6.97 %). At the higher concentration of 19.6 µM, the average peak current was 20.19±0.41 µA, with an RSD of 2.01 %, again lower than ½RSDH (6.19 %). These results demonstrate that the developed (1.0/1)NiF/ /GrO(S,N)/GCE sensor exhibits good repeatability and reliable analytical performance for SBT determination. The low RSD values obtained at different concentrations indicate that the proposed sensor provides stable and consistent electrochemical responses.

The reproducibility and long-term stability of the (1.0/1)NiF/GrO(S,N)/GCE sensor were further evaluated using SBT at an 8.9 µM concentration in 0.1 M BRS buffer solution (pH 3). To assess the reproducibility of electrode fabrication, seven modified electrodes were independently prepared using the same modification procedure and tested under identical conditions (Figure 12A).

The peak current obtained was 14.10±0.68 µA, with a relative standard deviation (RSD) of 4.85 %, indicating good reproducibility of the electrode preparation process. The long-term stability of the sensor was investigated over 7 days (Figure 12B). The peak current obtained during this period was 14.73±0.86 µA, with an RSD of 5.86 %, demonstrating that the modified electrode maintains stable electrochemical performance during storage. After 7 days, the peak current decreased by approximately 15 %, confirming the acceptable stability of the (1.0/1)NiF/GrO(S,N)/GCE sensor. These results indicate that the proposed sensor exhibits good reproducibility and satisfactory long-term stability, making it suitable for practical electrochemical detection of SBT.

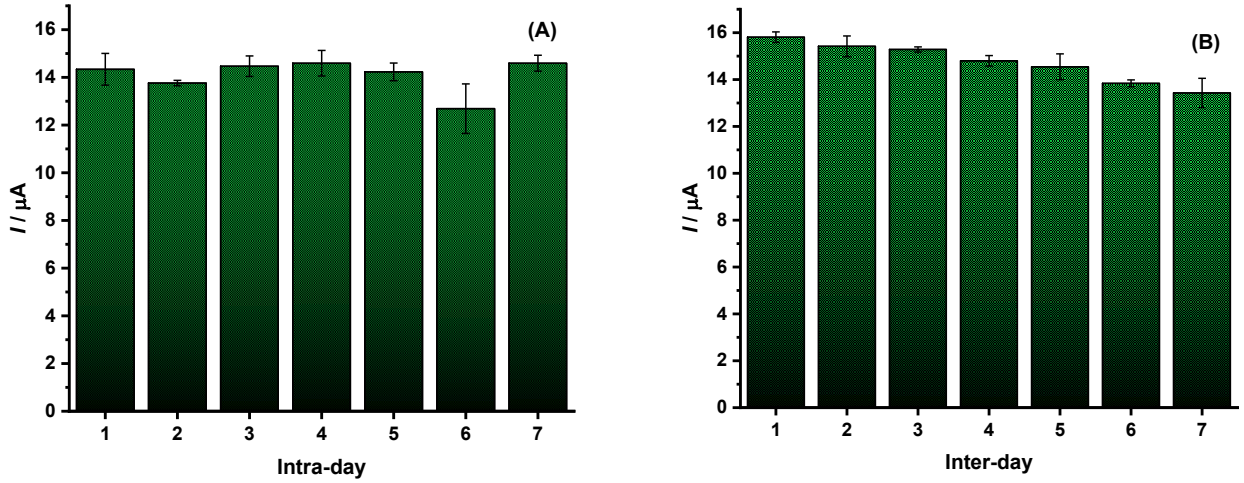

Figure 12. *Peak current responses for 8.9 µM SBT in 0.1 M BRS buffer solution (pH 3) obtained at (1.0/1)NiF/GrO(S,N)/GCE: A - reproducibility test using seven independently prepared electrodes; B - long-term stability test over seven days*

Interference study

The selectivity of the (1.0/1)NiF/GrO(S,N)/GCE sensor for SBT detection was assessed by evaluating the effects of various potential interfering substances on its performance. The interference study was conducted in a 0.1 M BRS buffer solution (pH 3) with SBT, and peak current changes were recorded in the presence of different interfering compounds at various concentration ratios compared to SBT. The tested substances included NaCl (C1), $ZnCl_2$ (C2), $(NH_4)_2SO_4$ (C3), NH_4NO_3 (C4), K_2SO_4 (C5), $Ca(HPO_4)_2$ (C6), urea (C7), saccharin (C8), caffeine (C9), sodium benzoate (C10), D-glucose (C11) and ascorbic acid (C12).

As shown in Figure 11D, most inorganic salts such as NaCl, $(NH_4)_2SO_4$, NH_4NO_3, K_2SO_4, and $Ca(HPO_4)_2$ exhibit negligible influence on the SBT peak current, even at concentration ratios up to 200 times higher than that of SBT, with signal deviations generally less than ±5 %. Similarly, organic compounds such as urea, caffeine, sodium benzoate, and D-glucose cause only minor changes in the peak current, indicating weak interference.

However, saccharin and ascorbic acid exhibit relatively stronger interference effects at higher concentration ratios, resulting in noticeable decreases in peak current. This behaviour may be attributed to their possible electrochemical activity or competitive adsorption on the electrode surface. Overall, the results demonstrate that the proposed (1.0/1)NiF/GrO(S,N)/GCE sensor exhibits good selectivity for SBT detection, with most common interfering substances exerting only minimal influence on the analytical signal.

Determination of SBT in real samples

The applicability of the proposed (1.0/1)NiF/GrO(S,N)/GCE sensor for practical analysis was evaluated by measuring SBT in seven commercial dietary supplement products. The results were compared with those from the reference HPLC method, and the accuracy of the proposed method was further validated using the standard addition technique. As shown in Table 3, the SBT contents measured by the DPV method closely match those obtained by HPLC, indicating the reliability of the electrochemical approach. The SBT levels in the tested products ranged from 10.10 to 20.18 mg per package, depending on the product formulation. To assess accuracy, a known amount of SBT (2.798 µg) was added to the sample solutions. The recoveries ranged from 96.38 to 104.83 %, with acceptable standard deviations. These results fall within the typical range for analytical methods (90 to 110 %), confirming the method's accuracy. Overall, the results demonstrate that the (1.0/1)NiF/ /GrO(S,N)/GCE sensor offers reliable and precise detection of SBT in real dietary supplement samples without significant matrix interference, highlighting its potential for practical use in food and pharmaceutical testing.

Table 3. *Determination of SBT in commercial dietary supplement samples using the proposed DPV method and comparison with the HPLC method. The amount of STB added was 1.3990 µg*

Sample	SBT content ± SD, mg *per* package		Found mount of STB ± SD, µg	Recovery, %
	HPLC*	DPV**		
#1	20.18 ± 0.45	20.36 ± 0.44	1.4546 ± 0.0321	103.98
#2	16.64 ± 0.28	16.40 ± 0.52	1.4369 ± 0.0463	102.71
#3	10.41 ± 0.31	10.11 ± 0.31	1.3503 ± 0.0386	96.52
#4	10.69 ± 0.15	10.83 ± 0.23	1.3638 ± 0.0293	97.49
#5	15.18 ± 0.39	14.78 ± 0.52	1.4316 ± 0.0452	102.33
#6	13.67 ± 0.26	13.86 ± 0.36	1.4567 ± 0.0488	104.13
#7	14.84 ± 0.54	15.14 ± 0.58	1.3756 ± 0.0564	98.25

*determined by the reference HPLC method; **determined by the proposed DPV method using NF-(N&S)GO/GCE

Conclusion

In this work, a $NiFe_2O_4$/S,N-doped graphene oxide composite (NiF/GrO(S,N) was successfully synthesized and used as an electrochemical sensing material for SBT detection. Structural and physicochemical characterizations confirmed the formation of nanocrystalline $NiFe_2O_4$ particles uniformly anchored on S,N-doped graphene sheets, yielding a hybrid structure with increased surface area and abundant active sites.

The NiF/GrO(S,N)/GCE-modified electrode showed significantly improved electrocatalytic activity toward SBT oxidation compared to other modified electrodes. The proposed sensor offered a wide

(cc) BY

linear range, low detection limit, good repeatability, reproducibility, and reliable long-term stability. Additionally, the sensor demonstrated good selectivity against common interfering substances. The developed method was successfully used to measure SBT in commercial dietary supplement products, and the results closely matched those obtained with the reference HPLC method. Therefore, the proposed NiF/GrO(S,N)/GCE sensor is a simple, sensitive, and reliable electrochemical platform for detecting SBT in real samples and has potential uses in food and pharmaceutical analysis.

Supplementary material

Additional data are available at https://pub.iapchem.org/ojs/index.php/JESE/article/view/3318, or from the corresponding author on request.

Contribution statement: *N.T.T. Xuan, L.T.T. Nhi and N.Q. Man: conceptualization, methodology, investigation, formal analysis, funding acquisition, writing original draft; V.T.K. Linh and N.H. Phong: supervision, validation; D.Q. Khieu, L.L. Son, L.T.H. Phong and P.K. Lieu: supervision, writing, review & editing. All authors read and approved the final manuscript.*

Conflict of Interests: *None*

Acknowledgment*: The authors thank Hue University for their financial support under the Core Research Program No. NCTB.DHH.2025.05.*

References

[1] C. Cercato, M. A. M. Stumpf, G. N. da Cunha Freire, E. Z. Kawahara, A. E. Fernandes, M. E. de Melo, M. C. Mancini, Combination of sibutramine and topiramate for the treatment of obesity: the SIBAMATE retrospective cohort study, *Diabetology & Metabolic Syndrome* **17** (2025) 289. https://doi.org/10.1186/s13098-025-01842-1

[2] W. P. T. James, I. D. Caterson, W. Coutinho, N. Finer, L. F. Van Gaal, A. P. Maggioni, C. Torp-Pedersen, A. M. Sharma, G. M. Shepherd, R. A. Rode, C. L. Renz, Effect of Sibutramine on Cardiovascular Outcomes in Overweight and Obese Subjects, *The New England Journal of Medicine* **363** (2010) 905-917. https://doi.org/10.1056/NEJMoa1003114

[3] M. F. Santillo, R. L. Sprando, Safety pharmacology of sibutramine analogues evaluated by in silico and in vitro biological target screening, *Chemico-Biological Interactions* **420** (2025) 111669. https://doi.org/10.1016/j.cbi.2025.111669

[4] A. A. Jairoun, S. S. Al-Hemyari, M. Shahwan, S. H. Zyoud, Adulteration of Weight Loss Supplements by the Illegal Addition of Synthetic Pharmaceuticals, *Molecules* **26** (2021) 6903. https://doi.org/10.3390/molecules26226903

[5] L. Manning, M. Bieniek, A. Kowalska, R. Ward, Dietary supplements, harm associated with synthetic adulterants and potential governance solutions, *Crime, Law and Social Change* **78** (2022) 507-533. https://doi.org/10.1007/s10611-021-09992-9

[6] A. Gürbüzer, H. İ. Ulusoy, İ. Narin, Sensitive Detection of Sibutramine and Fluoxetine Adulteration in Herbal Slimming Products by Means of Using Magnetic Solid Phase Extraction Combined with HPLC-DAD, *Food Analytical Methods* **18** (2025) 459-470. https://doi.org/10.1007/s12161-024-02711-9

[7] B. Sezgin, M. Soyseven, G. Arli, Multi-Metric Evaluation of a Green HPLC-PDA Method for Sibutramine Quantification in Herbal Teas, *Biomedical Chromatography* **40** (2026) e70318. https://doi.org/10.1002/bmc.70318

[8] J.-W. Bae, C.-I. Choi, C.-G. Jang, S.-Y. Lee, Simultaneous determination of sibutramine and its active metabolites in human plasma by LC-MS/MS and its application to a pharmacokinetic study, *Biomedical Chromatography* **25** (2011) 1181-1188. https://doi.org/10.1002/bmc.1587

[9] L. Du, Y. Wang, X. Li, M. Du, L. Zhu, J. Su, H. Wang, W. Gong, Determination of sibutramine and metabolites M1 and M2 in human blood and tissue samples by LC-MS/MS and its forensic application, *Australian Journal of Forensic Sciences* **58** (2026) 201-213. https://doi.org/10.1080/00450618.2025.2503801

[10] Y. Altunkaynak, G. Önal, A. Levent, Application of boron-doped diamond electrode for rapid and sensitive voltammetric detection of vildagliptin in anionic surfactant medium, *Monatshefte Für Chemie - Chemical Monthly* **154** (2023) 181-190. https://doi.org/10.1007/s00706-022-03020-9

[11] A. Levent, Voltammetric behavior of acebutolol on pencil graphite electrode: highly sensitive determination in real samples by square-wave anodic stripping voltammetry, *Journal of the Iranian Chemical Society* **14** (2017) 2495-2502. https://doi.org/10.1007/s13738-017-1184-z

[12] A. Çağıl, G. Doğan, A. Levent, Analysis of foodstuffs for the determination of Fluopyram by square wave voltammetry using a glassy carbon electrode, *Journal of Food Composition and Analysis* **139** (2025) 107070. https://doi.org/10.1016/j.jfca.2024.107070

[13] A. Kul, F. Budak, A. Cetinkaya, S. I. Kaya, S. Al, O. Sagirli, S. A. Ozkan, Fabrication of a molecularly imprinted polymer-based electrochemical sensor for the selective assay of antipsychotic drug clozapine and performance comparison with LC-MS/MS, *Talanta* **281** (2025) 126810. https://doi.org/10.1016/j.talanta.2024.126810

[14] A. Kiliç, M. Aslan, A. Levent, Investigation of the electrochemical properties of edoxaban using glassy carbon and boron-doped diamond electrodes and development of an eco-friendly and cost effective voltammetric method for its determination, *Analytical Biochemistry* **685** (2024) 115386. https://doi.org/10.1016/j.ab.2023.115386

[15] U. Pengsomjit, F. Alabdo, C. Karuwan, C. Kraiya, W. Alahmad, S.A. Ozkan, Innovative Graphene-Based Nanocomposites for Improvement of Electrochemical Sensors: Synthesis, Characterization, and Applications, *Critical Reviews in Analytical Chemistry* **55** (2025) 1259-1277. https://doi.org/10.1080/10408347.2024.2343854

[16] S. Ozbey, G. Keles, S. Kurbanoglu, Innovations in graphene-based electrochemical biosensors in healthcare applications, *Microchimica Acta* **192** (2025) 290. https://doi.org/10.1007/s00604-025-07141-w

[17] Q. Ran, F. Sheng, G. Chang, M. Zhong, S. Xu, Sulfur-doped reduced graphene oxide@chitosan composite for the selective and sensitive electrochemical detection of Hg^{2+} in fish muscle, *Microchemical Journal* **175** (2022) 107138. https://doi.org/10.1016/j.microc.2021.107138

[18] X. Chen, Y. Qi, B. Liu, X. Qiu, X. Lin, Y. Qin, Structural optimization of the $NiFe_2O_4$ spinel catalyst aimed at efficient electrocatalytic C-O bond cleavage of lignin, *Chemical Engineering Science* **301** (2025) 120722. https://doi.org/10.1016/j.ces.2024.120722

[19] M. A. Fadil, R. M. A. Hameed, G. G. Mohamed, O. A. Fouad. $NiFe_2O_4$ Nanoparticles as Highly Sensitive Electrochemical Sensor for Nitrite Determination, *Applied Organometallic Chemistry* **39** (2025) e70043. https://doi.org/10.1002/aoc.70043

[20] R. Biswal, P. Yadav, P. Mishra, P. Kumar, M. K. Singh, A comprehensive study of $NiFe_2O_4$ and $NiFe_2O_4$/rGO (reduced graphene oxide) nanocomposite: synthesis, structural, optical, dielectric, magnetic and magneto-dielectric analysis, *Journal of Materials Science: Materials in Electronics* **35** (2024) 868. https://doi.org/10.1007/s10854-024-12612-6

[21] M. Hodlevska, V. Kotsyubynsky, V. Boychuk, I. Budzulyak, B. Rachiy, R. Zapukhlyak, M. Hodlevsky, L. Turovska, Hydrothermally synthesized $NiFe_2O_4$/rGO composites: structure, morphology and electrical conductivity, *Applied Nanoscience* **13** (2023) 5199-5209. https://doi.org/10.1007/s13204-022-02741-x

[22] D. C. Marcano, D. V. Kosynkin, J. M. Berlin, A. Sinitskii, Z. Sun, A. Slesarev, L. B. Alemany, W. Lu, J. M. Tour, Improved Synthesis of Graphene Oxide, *ACS Nano* **4** (2010) 4806-4814. https://doi.org/10.1021/nn1006368

(cc) BY

[23] M. B. Askari, P. Salarizadeh, Binary nickel ferrite oxide ($NiFe_2O_4$) nanoparticles coated on reduced graphene oxide as stable and high-performance asymmetric supercapacitor electrode material, *International Journal of Hydrogen Energy* **45** (2020) 27482-27491. https://doi.org/10.1016/j.ijhydene.2020.07.063

[24] M. S. Amir Faiz, C. A. Che Azurahanim, S. A. Raba'ah, M. Z. Ruzniza, Low cost and green approach in the reduction of graphene oxide (GO) using palm oil leaves extract for potential in industrial applications, *Results in Physics* **16** (2020) 102954. https://doi.org/10.1016/j.rinp.2020.102954

[25] A. Soam, R. Kumar, D. Thatoi, M. Singh, Electrochemical Performance and Working Voltage Optimization of Nickel Ferrite/Graphene Composite based Supercapacitor, *Journal of Inorganic and Organometallic Polymers and Materials* **30** (2020) 3325-3331. https://doi.org/10.1007/s10904-020-01540-7

[26] J.-B. Wu, M.-L. Lin, X. Cong, H.-N. Liu, P.-H. Tan, Raman spectroscopy of graphene-based materials and its applications in related devices, *Chemical Society Reviews* **47** (2018) 1822-1873. https://doi.org/10.1039/C6CS00915H

[27] T. F. Emiru, D. W. Ayele, Controlled synthesis, characterization and reduction of graphene oxide: A convenient method for large scale production, *Egyptian Journal of Basic and Applied Sciences* **4** (2017) 74-79. https://doi.org/10.1016/j.ejbas.2016.11.002

[28] R. A. Rochman, S. Wahyuningsih, A. H. Ramelan, Q.A. Hanif, Preparation of nitrogen and sulphur Co-doped reduced graphene oxide (rGO-NS) using N and S heteroatom of thiourea, *IOP Conference Series: Materials Science and Engineering* **509** (2019) 12119. https://doi.org/10.1088/1757-899X/509/1/012119

[29] J. Lu, Y. Li, S. Li, S.P. Jiang, Self-assembled platinum nanoparticles on sulfonic acid-grafted graphene as effective electrocatalysts for methanol oxidation in direct methanol fuel cells, *Scientific Reports* **6** (2016) 215301. https://doi.org/10.1038/srep21530

[30] A. J. Bard, L. R. Faulkner, *Electrochemical Methods: Fundamentals and Applications, 2nd Edition,* J. Wiley & Sons, 2001, 580-632. ISBN: 978-1-118-31280-3. https://www.wiley.com/en-be/shop/general-chemistry/electrochemical-methods-fundamentals-and-applications-2nd-edition-p-9781118312803

[31] E. Laviron, General expression of the linear potential sweep voltammogram in the case of diffusionless electrochemical systems, *Journal of Electroanalytical Chemistry and Interfacial Electrochemistry* **101** (1979) 19-28. https://doi.org/10.1016/S0022-0728(79)80075-3

[32] J. Soleymani, M. Hasanzadeh, N. Shadjou, M. Khoubnasab Jafari, J.V. Gharamaleki, M. Yadollahi, A. Jouyban, A new kinetic-mechanistic approach to elucidate electrooxidation of doxorubicin hydrochloride in unprocessed human fluids using magnetic graphene based nanocomposite modified glassy carbon electrode, *Materials Science & Engineering: C* **61** (2016) 638-650. https://doi.org/10.1016/j.msec.2016.01.003

[33] C. Li, Electrochemical determination of dipyridamole at a carbon paste electrode using cetyltrimethyl ammonium bromide as enhancing element, *Colloids and Surfaces B* **55** (2007) 77-83. https://doi.org/10.1016/j.colsurfb.2006.11.009

[34] A. Kongsuwan, S. Chuenjitt, C. H. Phua, S. Wangchuk, J. Saichanapan, K. Saisahas, K. Samoson, A. Soleh, K. Promsuwan, W. Limbut, Sibutramine detection in weight-loss products using a sodium/phosphorus dual-doped carbon nanotubes modified electrode, *Microchemical Journal* **190** (2023) 108668. https://doi.org/10.1016/j.microc.2023.108668

[35] A. B. Lima, W. T. P. dos Santos, R. G. Compton, Simple and Sensitive Determination of Sibutramine in Slimming Tea Beverages Using a Carbon Screen-printed Electrode with Adsorptive Stripping Voltammetry, *Electroanalysis* **31** (2019) 975-980. https://doi.org/10.1002/elan.201800888

[36] J. M. Carvalho, A. R. Da Silva, A. L. M. C. Da Cunha, R. Q. Aucélio, M. A. André Luis, C. L. Katia, Voltammetric determination of sibutramine in beverages and in pharmaceutical formulations, *Quimica Nova* **35** (2012) 988-992. https://doi.org/10.1590/S0100-40422012000500023

[37] N. A. El Gohary, R. M. El Nashar, H. Y. Aboul-Enien, Potentiometric Determination of Sibutramine Using Batch and Flow Injection Analysis, *Analytical Letters* **44** (2011) 241-257. https://doi.org/10.1080/00032719.2010.500760

[38] J. M. Freitas, T. C. Oliveira, M. H. P. Santana, C. E. Banks, R. A. A. Munoz, E.M. Richter, A simple and fast-portable method for the screening of the appetite-suppressant drug sibutramine in natural products and multivitamins supplements, *Sensors and Actuators B* **282** (2019) 449-456. https://doi.org/10.1016/j.snb.2018.11.094

[39] K. Sirivibulkovit, P. Wilairat, D. Nacapricha, S. Wichit, P. Saetear, A simple cost-effective paper-based electrochemical device for detection of adulterated sibutramine in slimming products, *Analytical Methods* **14** (2022) 2461-2470. https://doi.org/10.1039/D2AY00585A

©2026 by the authors; licensee IAPC, Zagreb, Croatia. This article is an open-access article distributed under the terms and conditions of the Creative Commons Attribution license (http://creativecommons.org/licenses/by/4.0/)